

1 Ion heating in the polar cap under northwards IMF Bz

2 Leslie J. Lamarche¹, Roger H. Varney¹, and Ashton S. Reimer¹

3 ¹SRI International, Menlo Park, CA, USA

4 Key Points:

- 5 • Ion temperature enhancements are frequently observed in the noon sector of the
6 polar cap under IMF north conditions
- 7 • Current models driven by large-scale convection and precipitation fail to produce
8 the observed ion temperature enhancements
- 9 • Mesoscale flows and precipitation structures may be critical to account for ion heat-
10 ing in the polar cap

Abstract

Joule heating deposits a significant amount of energy into the high-latitude ionosphere and is an important factor in many magnetosphere-ionosphere-thermosphere coupling processes. Although the interplanetary magnetic field (IMF) is known to impact the Joule heating pattern across the entire polar cap ionosphere, it is less clear how it influences specific localized heating events. We consider the relationship between localized temperature enhancements in polar cap measured with the Resolute Bay Incoherent Scatter Radar-North (RISR-N) and the orientation of the IMF. Based on analysis of 10 years of data, RISR-N most commonly observes ion heating in the noon sector under northwards IMF B_z . We interpret heating events in that sector as being primarily driven by electric fields associated with lobe reconnection. We attempt to model two of the observed temperature enhancements with a data-driven first principles regional model of ionospheric plasma transport and dynamics, but fail to fully reproduce the ion temperature enhancements. However, evaluating the ion energy equation using the locally measured ion velocities reproduces the observed ion temperature enhancements. This result indicates that current techniques for estimating global electric fields are not adequately capturing mesoscale electric fields in the polar cap, and this can result in underestimation of the energy deposition into the ionosphere and thermosphere.

1 Introduction

Joule heating in the polar cap F-region ionosphere is a significant factor in magnetosphere-ionosphere coupling. Magnetic reconnection between the interplanetary magnetic field (IMF) and the Earth's magnetosphere drives strong plasma convection across the entire polar region (Dungey, 1961). A relative velocity between ionized species and neutral species increases collisions between the two and heats both the plasma and neutral populations (Thayer et al., 1995; Fujii et al., 1999; Thayer & Semeter, 2004; Aikio et al., 2012). Plasma temperature enhancements have been connected to ion upflow, which contributes to the outflow of ionospheric plasma into the magnetosphere (Wahlund et al., 1992; Skjæveland et al., 2011). Ion outflow from the polar ionosphere has been identified as a significant source of cold-ion transport into the ring current and plasma sheet (Peterson et al., 2009; Li et al., 2013), resulting in mass loading of the magnetosphere (Moore & Horwitz, 2007; Li et al., 2012).

42 Joule heating is most significant in the cusp and auroral regions at high latitudes
43 (Foster & St.-Maurice, 1983; Olsson et al., 2004; Aikio & Selkälä, 2009), however, it has
44 been identified as the dominate form of energy input into the polar cap, particularly dur-
45 ing active periods (Lu et al., 2016). Joule heating is estimated to be responsible for 50%-
46 60% of the global storm-time energy budget (Tanskanen et al., 2002; Østgaard et al., 2002;
47 Knipp et al., 1998). The IMF orientation can also impact Joule heating at high latitudes,
48 in addition to broader ion transport processes (McHarg et al., 2005; Howarth & Yau, 2008;
49 Yau et al., 2012; Cai et al., 2014). Extensive statistical surveys of the entire high-latitude
50 region have resulted in empirical models of Joule heating patterns parameterized by IMF
51 conditions and geomagnetic indices (Chun et al., 2002; Palmroth et al., 2005; X. X. Zhang
52 et al., 2005), however, these are mostly useful to gain insight on the average large-scale
53 behavior and are not designed to predict localized heating events.

54 Time-varying magnetic reconnection at the magnetopause can drive heating events
55 in the ionosphere (Moen et al., 2004; Lockwood et al., 2005). In particular, northwards
56 IMF moves the reconnection point from close to the sun-earth line to the lobe of the mag-
57 netosphere, which significantly changes the ionospheric convection pattern (Burke et al.,
58 1979; Cowley, 1983). The resulting pattern often has three or more cells and is highly
59 asymmetric (particularly if there is also a strong IMF B_y component) (Reiff & Heelis,
60 1994; Förster, Haaland, et al., 2008; Cousins & Shepherd, 2010; Thomas & Sheperd, 2018).
61 These patterns can cause strong flow channels in the dayside polar cap, which may be
62 responsible for significant localized Joule heating events.

63 This study will examine the relationship between the IMF orientation and local-
64 ized ion temperature enhancements in the polar cap ionosphere. In addition to a sta-
65 tistical analysis of ion temperature, we will attempt to model several observed Joule heat-
66 ing events to gain more insight as to what geophysical parameters and processes con-
67 tribute to localized heating in the polar cap.

68 **2 Methodology**

69 **2.1 RISR-N**

70 The Resolute Bay Incoherent Scatter Radar - North (RISR-N) is an Advanced Mod-
71 ular Incoherent Scatter Radar (AMISR) located deep within the northern polar cap (Kelly
72 & Heinselman, 2009; Bahcivan et al., 2010). At 82°N magnetic latitude (74.7°N, 94.9°W

geodetic) with a boresight directed roughly towards the magnetic pole, RISR-N is ideally located to observe open field line plasma dynamics. By employing electronic beam steering, RISR-N can quickly cycle through multiple look directions within its field of view to measure electron density, ion and electron temperature, and line-of-sight plasma velocity in a 3D volume in the ionosphere. RISR-N first began collecting science data in 2009 and operated roughly 5-10 days per month between 2009-2018. In September 2018, a new smaller generator was installed at the site (in addition to the main generator) to power the radar, which allows much more flexibility in scheduling operations and observation time. One advantage of this has been several month-long periods of almost continuous low duty cycle radar operations since the beginning of 2019.

This study focuses on F-region dynamics so only long pulse data are presented. The standard AMISR processing routine gates the lag product array into autocorrelation functions, and determines the plasma parameters within each range gate through nonlinear least squares fitting of the autocorrelation functions. This analysis assumes the fitted parameters are slowly varying in range over the pulse length and in time over the integration period. Most standard modes have a range resolution between 49-72 km and a minimum integration period of 1-3 minutes. The data-model comparisons shown later in this study use special Topside modes, which are optimized for observing dynamics in the topside F-region. These topside modes use only 5 beam positions in order to increase the number of samples in each beam compared to more typical RISR-N modes using 11 to 52 beam positions. The topside modes interleave long pulses of different lengths, although this manuscript will only discuss parameters derived from the 480 μ s pulses (72 km range spreading) using the standard AMISR processing.

2.2 IPWM

The Ionosphere/Polar Wind model (IPWM) is a 3D plasma transport model designed for high latitudes (Varney et al., 2015, 2016). It solves the 8-moment equations for the parallel transport of H^+ , He^+ , O^+ (^4S), and electrons. Photochemistry for the species N^+ , NO^+ , N_2^+ , O_2^+ , O^+ (^2D), and O^+ (^2P) is also included. The model includes a kinetic electron solver, but it has been disabled for the simulations done in this study. Details on the parallel transport and chemistry schemes can be found in Varney et al. (2014) and a description of perpendicular transport is available in Varney et al. (2015). IPWM assumes no neutral winds, but the density and temperature of neutral species are

105 takes from the Naval Research Laboratory’s Mass Spectrometer Incoherent Scatter Radar
106 Extended (NRLMSISE-00) empirical model (Picone et al., 2002). NRLMSISE-00 is driven
107 by the F10.7 solar radio flux, a proxy for solar extreme ultraviolet radiation, and the Ap
108 geomagnetic index. The solar EUV spectra is provided by a high-resolution solar EUV
109 irradiance model for aeronomic calculations (HEUVAC) (Richards et al., 2006) and the
110 model calculates production and heating from precipitation with the empirical relation-
111 ships found in Fang et al. (2008).

112 IPWM uses a nonorthogonal magnetic-centered dipole Eulerian grid. The grid is
113 constructed from surfaces of constant L shell, MLT, and altitude. The lower boundary
114 is set at 97 km by chemical equilibrium while the upper boundary is open at 8400 km.
115 The equatorward boundary (set at L=4) is treated as a hard wall with no transport from
116 lower latitudes. All simulations shown in this paper use spatial resolution of 2° in dipole
117 magnetic latitude and output parameters at a temporal resolution of 1 minute.

118 IPWM requires high-latitude energetic particle precipitation and electrostatic po-
119 tential patterns as inputs. Past work with IPWM has always used magnetospheric sim-
120 ulations to set these inputs (Varney et al., 2016). In contrast, in this work, simulations
121 will be driven by precipitation patterns derived from the Ovation Prime empirical model
122 (Newell et al., 2009). Ovation Prime outputs the number flux and average energy of mo-
123 noenergetic and broadband precipitation for a requested magnetic latitude and MLT at
124 high latitudes. The model is based on data from the DMSP SSJ/4 electrostatic analyz-
125 ers (Hardy et al., 1984, 2008) and is parameterized by solar wind conditions.

126 This study considers two independent sources of the high-latitude electrostatic po-
127 tential: SuperDARN and AMPERE. The Super Dual Auroral Radar Network (Super-
128 DARN) consists of about 30 ground-based high-frequency coherent-scatter radars at mid-
129 , high-, and polar latitudes (Greenwald et al., 1995; Chisham et al., 2007). Each radar
130 makes independent line-of-sight measurements of the plasma velocity, but convection maps
131 covering the entire polar region can be created by combining all measurements from a
132 particular time with climatological models of convection patterns based on geophysical
133 parameters such as the IMF and dipole tilt angle (Greenwald et al., 1995; Cousins & Shep-
134 herd, 2010; Thomas & Sheperd, 2018). The Active Magnetosphere and Planetary Elec-
135 trodynamics Response Experiment (AMPERE) uses magnetic field data from the Irid-
136 ium satellites to derive the global Birkeland current distributions (Waters et al., 2001;

137 Anderson et al., 2014). The Iridium Communications constellation consists of around
 138 70 near-polar orbiting satellites, each carrying engineering magnetometers. Cross-track
 139 magnetic field perturbations can be inverted to determine field-aligned currents (Anderson
 140 et al., 2000; Waters et al., 2001). From AMPERE current distributions, it is possible to
 141 derive the electrostatic potential by assuming constant conductance across the polar cap
 142 (Richmond & Kamide, 1988; Cousins et al., 2015). Because SuperDARN and AMPERE
 143 electrostatic potential maps are based on two independent data sources and involve dif-
 144 ferent assumptions, there can be significant differences between the two (Cousins et al.,
 145 2015). It is challenging to determine which is more accurate for any given period, so two
 146 IPWM simulations were run for each event discussed in this paper, one driven by Su-
 147 perDARN potential patterns and one by AMPERE.

148 **3 Results**

149 **3.1 Statistical Analysis of Ion Temperature Enhancements**

150 We performed a statistical analysis of ion temperature over the entire RISR-N database
 151 in order to determine which conditions most commonly produced ion heating. The database
 152 consists of all 5-minute-integrated long-pulse data collected by RISR-N between January
 153 2010 and February 2020. For each experiment, we filter out points where the AMISR
 154 fitting procedure is expected to have failed or where the ion temperature error exceeds
 155 1000 K. Failed fits are detected by checking if the exit code from the Levenberg-Marquardt
 156 algorithm, which performs the nonlinear least-squares fitting, does not indicate success-
 157 ful convergence, or if the normalized chi-squared statistic is less than 0.1 or greater than
 158 10. Then we extract the median ion temperature between 300–400 km altitude in the
 159 highest elevation beam within the grating lobe limit of the radar’s field-of-view. Above
 160 300 km, the AMISR fitting procedure assumes the ion composition is entirely O^+ . For
 161 experiments where the database does not include 5-minute-integrated files, we post-integrate
 162 1-minute data to 5 minutes by taking an error weighted average in time after the initial
 163 “failed fit” filter, then removing any points where the resulting weighted ion tempera-
 164 ture error is greater than 1000 K before finding the median temperature between 300-
 165 400 km altitude. After extracting the median F-region ion temperature for every long-
 166 pulse experiment, we bin these data by MLT (0.8 hour bins) and the IMF clock angle
 167 (12° bins) using one-hour resolution OMNI data and calculate the average temperature
 168 in each bin. The results are plotted in Figure 1a. Note that the IMF clock angle is de-

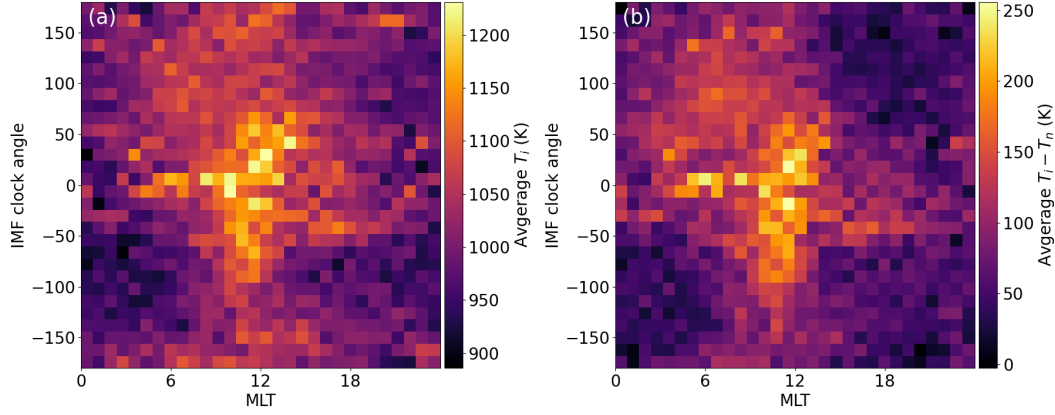


Figure 1. a) Average ion temperature observed by RISR-N per MLT sector and IMF clock angle (θ_c), and b) Average ion temperature minus NRLMSISE-00 neutral temperature per MLT sector and IMF clock angle. A clock angle of zero indicates northwards IMF.

169 fined as $\theta_c = \arctan By/Bz$ such that $\theta_c = 0^\circ$ corresponds to the IMF directed north-
 170 wards. In order to detrend diurnal, seasonal, and solar cycle variations in the neutral at-
 171 mosphere, we have also computed the average of $(T_i - T_n)$ using neutral temperatures,
 172 T_n , from NRLMSISE-00 (Picone et al., 2002).

173 Figure 1a shows that on average, RISR-N observes higher ion temperatures in the
 174 noon sector, particularly when the IMF has a significant northwards component ($\theta_c =$
 175 0°). Furthermore, Figure 1b demonstrates that this pattern persists even after subtract-
 176 ing NRLMSISE-00 neutral temperature. At 12 MLT, RISR-N is located just polewards
 177 of the cusp (B. Zhang et al., 2013). This region often experiences fast plasma flows, par-
 178 ticularly under northwards IMF conditions when magnetic reconnection occurs in the
 179 lobe of the magnetosphere driving 4-cell or asymmetric convection patterns in the iono-
 180 sphere. It should be clarified that these are flows in the polar cap and not associated with
 181 the bursty reconnection flows that occur in the cusp (Prikryl et al., 2002; Provan et al.,
 182 2002; Farugia et al., 2004). The elevated average ion temperature observed under these
 183 conditions may be due to an increased likelihood of RISR-N observing a Joule heating
 184 event due to fast sunward flows in the plasma driven by lobe reconnection.

185 The database contains several large heating events at local times away from 12 MLT,
 186 many of which are directly related to large geomagnetic storms. Most of these storm events,
 187 however, end up being statistical outliers in their particular MLT and IMF clock angle
 188 bin. Note that our analysis only sorts by IMF clock angle, and not IMF magnitude. The

189 few storm events with very large IMF magnitude and southwards clock angle do show
 190 elevated ion temperatures, but the relatively rarity of those events results in them not
 191 significantly contributing to the averages in Figure 1. The enhancement at 12 MLT and
 192 $\theta_c = 0^\circ$ in Figure 1 indicates that heating events under those conditions are very com-
 193 mon and are not confined to geomagnetic storm times.

194 **3.2 Modeling Joule Heating Events with IPWM**

195 We chose two particularly large ion heating events observed by RISR-N for detailed
 196 case studies: one in May 2014 and another in April 2016. The May 2014 event has been
 197 previously discussed by Shen et al. (2016), and it was also a large ion upflow event ob-
 198 served by the enhanced Polar Outflow Probe (e-POP). Both of these events occurred dur-
 199 ing IMF northwards conditions and both were observed using topside modes at RISR-
 200 N. These events both have ion temperatures significantly higher than the average ion tem-
 201 peratures in Figure 1, but neither is as extreme as the September 2014 event previously
 202 discussed by Clauer et al. (2016). We modeled both of these events using convection pat-
 203 terns from both SuperDARN and AMPERE, for a total of four simulations. Animations
 204 of all full runs are provided in the supplementary materials.

205 Figure 2 summarizes the heating observations made during the May 2014 event and
 206 the two simulations of this event. Figures 2c shows ion temperature measured in the RISR-
 207 N beam closest to vertical (80° elevation), and the upper two panels show the ion tem-
 208 perature along the field line in the model grid cell closest to Resolute Bay. The data are
 209 presented in UT, and at RISR-N MLT = UT-6, such that noon is 18 UT. The RISR-
 210 N measurements in Figure 2c show two strong ion temperature enhancements on May
 211 30, 2014, a broad one around 21 UT and a shorter but more intense one right before 22
 212 UT. Figure 3 is a snapshot of the SuperDARN electric potential (left) and Ovation Prime
 213 monoenergetic precipitation average energy and flux (center) used to drive IPWM, as
 214 well as the output ion temperature from IPWM at 300 km. All panels are in the native
 215 IPWM dipole grid with grey dashed lines showing dipole colatitude 10° and 20° off the
 216 pole. The location of RISR-N at each time is indicated with the black tripod. Figure 4
 217 has the same format as Figure 3, but is shown for a time during the second observed ion
 218 temperature enhancement right before 22 UT. For both time periods, the IMF has a strong
 219 northward component which restructured the ionospheric convection to produce a re-
 220 verse convection cell near RISR-N. During the first observed heating period around 21

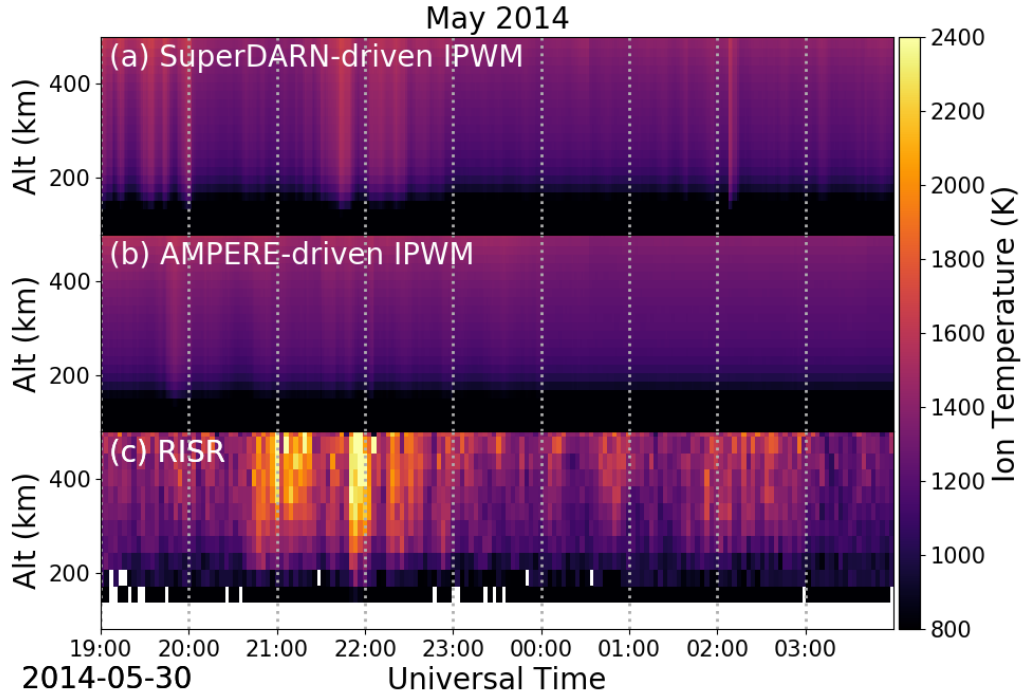


Figure 2. Modeled and observed ion temperature over Resolute Bay from May 30, 2014 19:00 UT to May 31, 2014 4:00 UT. Panel a shows the temperature modeled by IPWM driven by Ovation Prime precipitation and SuperDARN electric potential maps. Panel b shows the temperature modeled by IPWM driven by Ovation Prime precipitation and AMPERE electric potential maps. Panel c shows the ion temperature measured by RISR-N along the highest elevation beam.

221 UT (Figure 3), this reverse convection from SuperDARN is very weak, and IPWM did
 222 not produce any significant ion temperature enhancement. During the second period right
 223 before 22 UT (Figure 4), the SuperDARN reverse convection cell is more pronounced,
 224 and IPWM does generate some temperature enhancement. Nonetheless, this ion tem-
 225 perature enhancement is still substantially less than that measured by RISR-N.

226 Figure 5 summarizes the heating observations made during the April 2016 event
 227 and the two simulations of this event in the same format as Figure 2. The RISR-N ob-
 228 servations in Figure 5c show two distinct heating events: a short one on April 21, 2016
 229 around 19 UT and a much more extended event on April 22, 2016 between 17-20 UT.
 230 Neither SuperDARN-driven (Figure 5a) nor AMPERE-driven (Figure 5b) IPWM repro-
 231 duced the short temperature enhancement on April 21, 2016, however both showed some
 232 evidence of enhanced ion temperatures during the longer heating event on the next day.

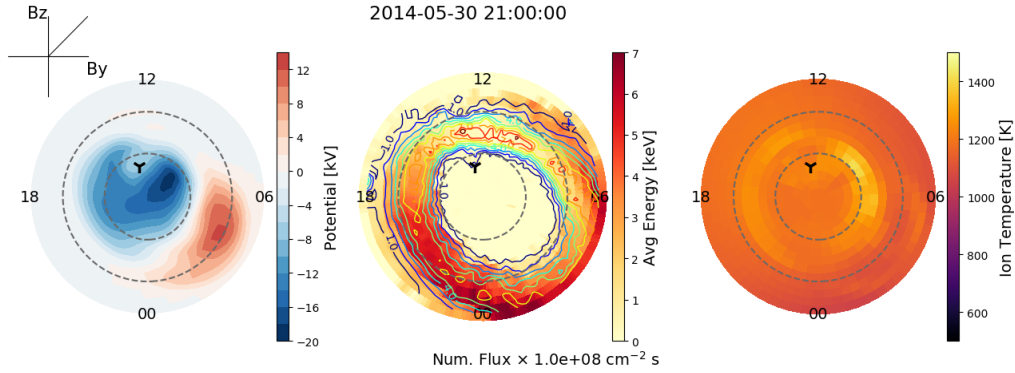


Figure 3. Snapshot of SuperDARN-driven IPWM run on May 30, 2014 at 21:00 UT. The left plot shows the electric potential used to drive IPWM at this time. The middle plot show the average energy (background color) and number flux (overlaid line contours) of the input monoenergetic particle precipitation from Ovation Prime. The right panel shows the modeled ion temperatures at 300 km. All panels are in the IPWM magnetic latitude/MLT grid. The two dashed grey circles indicate magnetic latitude 10° and 20° from the pole. The black tripod shows the location of RISR-N in each panel. IMF clock angle at this time is indicated in the top left corner.

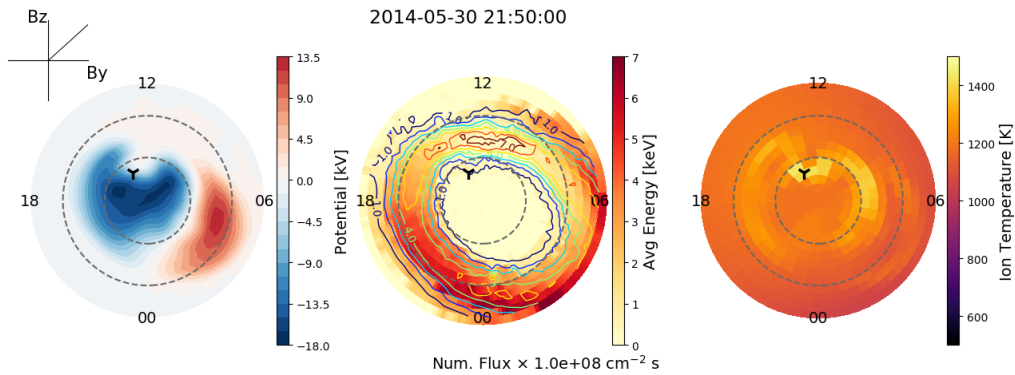


Figure 4. Snapshot of SuperDARN-driven IPWM run on May 30, 2014 at 21:50 UT. Figure format is the same as Figure 3.

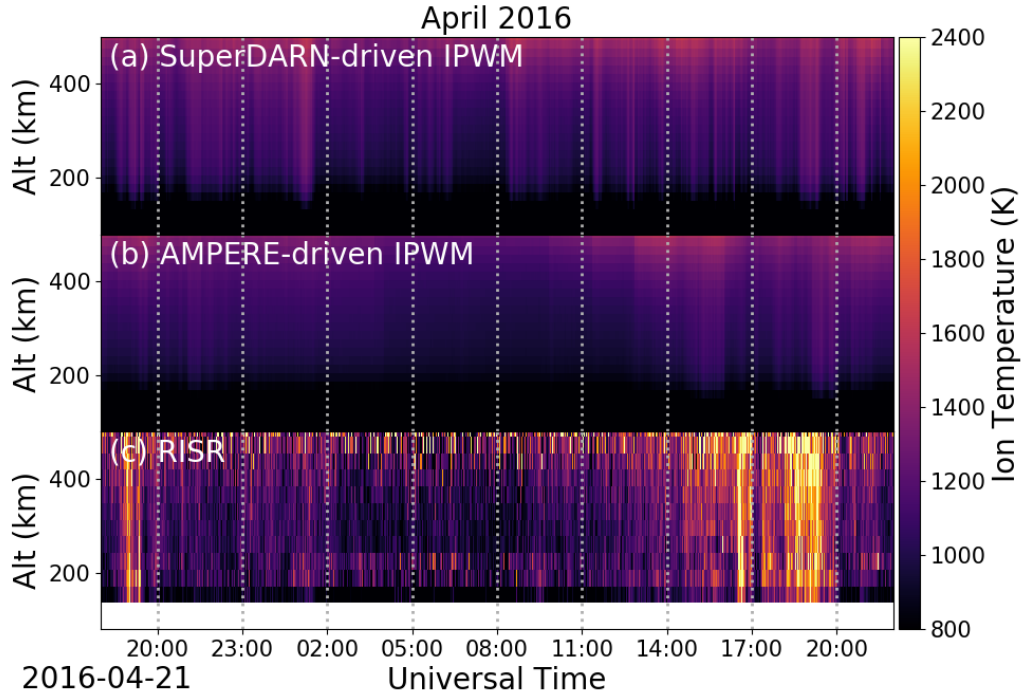


Figure 5. Modeled and observed ion temperature over Resolute Bay from April 21, 2016 18:00 UT to April 22, 2016 22:00 UT. Figure format same as Figure 2.

233 During this longer event, the IMF was northwards, but also had a significant By com-
 234 ponent, resulting in multi-celled and highly asymmetric convection patterns. A small tem-
 235 perature enhancement is seen in the vicinity of RISR-N in SuperDARN-driven IPWM
 236 at 19 UT (Figure 5a). As seen in Figure 6, this corresponds to a small region of dayside
 237 sunwards convection. A similar temperature enhancement is seen slightly later in the AMPERE-
 238 driven IPWM at around 19:30 UT (Figure 5b). In this case, the IMF is pointed almost
 239 entirely in the positive y direction, resulting in strong downward convection over RISR-
 240 N. It is important to note however that neither the SuperDARN-driven nor AMPERE-
 241 driven IPWM produced the duration or amplitude of the ion temperature enhancement
 242 observed in the RISR-N data.

243 4 Discussion

244 In the simulations shown in Section 3.2, IPWM is driven with measured convec-
 245 tion patterns from either SuperDARN or AMPERE, yet strongly underestimate the ob-
 246 served ion temperature enhancements. This suggests that there are either fundamental

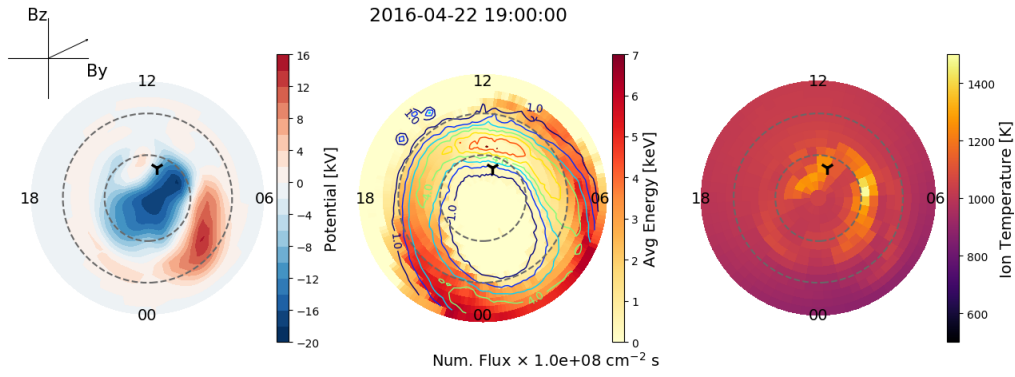


Figure 6. Snapshot of SuperDARN-driven IPWM run on April 22, 2016 at 19:00 UT. Figure format is the same as Figure 3.

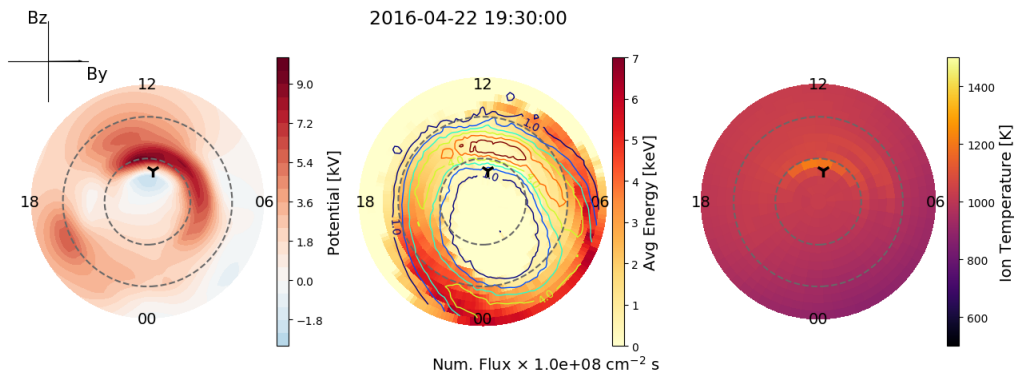


Figure 7. Snapshot of AMPERE-driven IPWM run on April 22, 2016 at 19:30 UT. Figure format is the same as Figure 3.

247 physics that are not being captured by IPWM or that the observation-based drivers do
 248 not adequately capture all important scales. In the F-region, Equation 1 is a reasonable
 249 approximation of the ion energy equation (St.-Maurice & Hanson, 1982).

$$T_i = T_n + \frac{m_n}{3k_B} |\vec{V}_i - \vec{V}_n|^2 \quad (1)$$

250 Here, T_i and T_n are the ion and neutral temperatures, respectively, m_n is the average
 251 mass of the neutral species, k_B is Boltzmann's constant, and \vec{V}_i and \vec{V}_n are the ion and
 252 neutral velocities, respectively. Although this expression describes frictional heating, Joule
 253 heating rates are equivalent to frictional heating rates under F-region assumptions (Thayer
 254 & Semeter, 2004). To first order in the F-region, the ion temperature is predominantly
 255 determined by the ion-neutral velocity difference.

256 Although both SuperDARN and AMPERE create data-derived convection patterns,
 257 neither system provides convection measurements with sufficient spatial resolution char-
 258 acterize small and meso-scale flows across the entire polar cap. It is possible that small
 259 and meso-scale flows are a significant source of heating in the polar cap ionosphere, con-
 260 tributing to the substantial temperature enhancements shown in Figures 2 and 5. Chen
 261 and Heelis (2018) tabulated a significant number of mesoscale (100-500 km) flow per-
 262 turbations over the background convection and concluded they were an additional source
 263 of frictional heating. In order to assess the importance of meso-scale fast flows in our two
 264 events, we examined the local velocity observations from RISR-N. RISR-N line-of-sight
 265 velocity measurements from different beams can be inverted to derive the vector $\vec{E} \times$
 266 \vec{B} plasma drift velocity by assuming the flow field varies slowly over the RISR-N field-
 267 of-view (Heinselmann & Nicolls, 2008). In both events, RISR-N locally observed faster
 268 ion velocities than predicted by either the SuperDARN or AMPERE global patterns.

269 We also considered the possible role of neutral winds. The IPWM simulations in
 270 this work ignore the background neutral wind field, effectively assuming the neutral species
 271 are stationary with respect to the plasma. A nonzero neutral wind will reduce the heat-
 272 ing rate if the neutral motion is aligned with the ion motion and enhance it if it opposes
 273 it, so neglecting the neutral wind should not result in a systematic underestimation of
 274 the ion temperature in all cases. Strong plasma velocity can drag the neutral atmosphere
 275 into a similar pattern through ion-neutral collisions (Richmond et al., 2003; Emmert et
 276 al., 2006; Förster, Rentz, et al., 2008). Billett et al. (2019) estimated the neutral wind
 277 response time to a change in plasma convection at high latitudes to be roughly 75–90

278 minutes, depending on the strength of the event. During the heating event shown in May
 279 2014, the IMF moved steadily from southwards to northwards about 2 hours before the
 280 event was observed while in the April 2016 event, the IMF was strongly northwards for
 281 several hours before the heating event, but then moved southwards at the end of the ob-
 282 served heating period. In the May 2014 event, it is possible that differences between the
 283 neutral atmosphere motion and the plasma motion enhanced Joule heating. This is less
 284 likely in the April 2016 event due to the extended period of consistent IMF before the
 285 event began.

286 In order to test the consistency of the RISR-N observed temperature enhancements
 287 with the locally-measured \vec{V}_i , we have evaluated Equation 1 using the RISR-N locally-
 288 measured \vec{V}_i and empirical models for T_n and \vec{V}_n . The neutral temperatures use Naval
 289 Research Laboratory’s Mass Spectrometer Incoherent Scatter Radar Extended (NRLMSISE-
 290 00) empirical model (Picone et al., 2002), and the neutral winds use the High-latitude
 291 Thermospheric Wind Model (HL-TWiM) (Dhadly et al., 2019). HL-TWiM is an empir-
 292 ical model of F-region neutral winds based on several decades of high-latitude ground-
 293 and space-based measurements, including Fabry-Perot Interferometer measurements from
 294 an instrument at the Resolute Bay Observatory, colocated with RISR-N.

295 In general, the ion temperature calculated from Equation 1 with accurate mesoscale
 296 flows matches the measured temperature enhancements substantially better than the IPWM
 297 runs shown in Figures 2 and 5. Figure 8a shows the geodetic eastwards components of
 298 the RISR-N ion velocity (V_i , green) and the HL-TWiM neutral velocity (V_n , purple) at
 299 300 km over Resolute Bay for the May 2014 event. Likewise, Figure 8b shows the geode-
 300 tic northwards components of these velocities. The green lines in Figures 8c and 9c show
 301 the ion temperature calculated with Equation 1 neglecting the neutral wind ($\vec{V}_n = 0$)
 302 while the purple lines are the same calculation using neutral winds from HL-TWiM. The
 303 black line in Figure 8c is the percent difference between the ion temperatures calculated
 304 with and without accounting for neutral wind, with positive values (blue) indicating the
 305 background neutral winds enhance T_i and negative values (red) indicating they dimin-
 306 ish T_i . Figure 8d shows the full temperature profile calculated over Resolute Bay with
 307 the RISR-N \vec{V}_i and HL-TWiM \vec{V}_n , and Figures 8e shows the T_i profiles directly measured
 308 by RISR-N. Figure 9 shows the same calculations for the April 2016 event in the same
 309 format as 8.

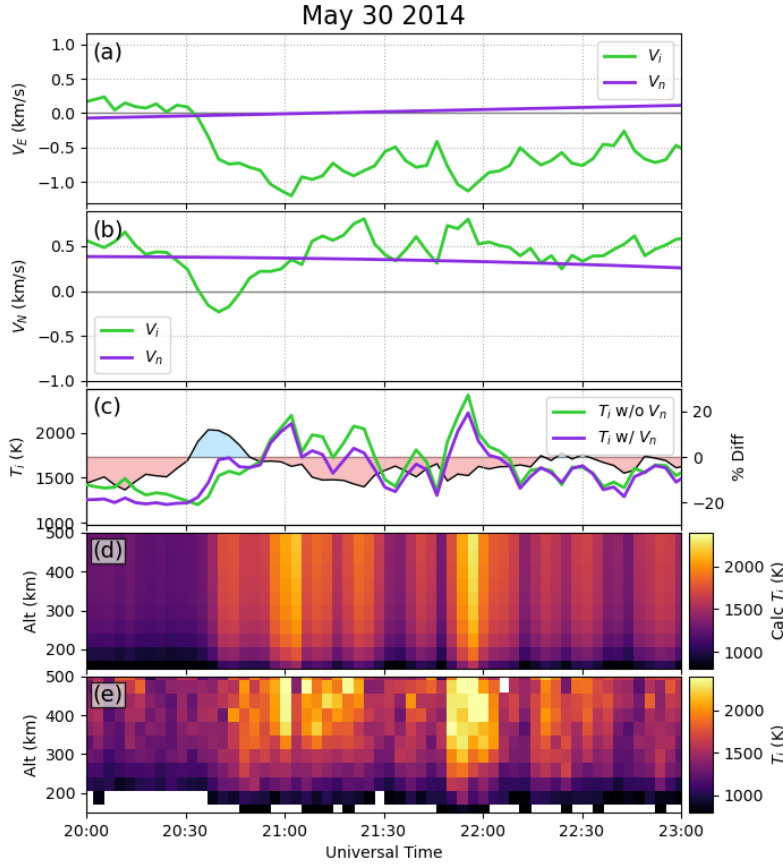


Figure 8. Comparison of the ion temperature calculated from RISR-N parameters with Equation 1 with the actual observed ion temperature for the May 2014 heating event. Panels a and b show the geodetic northwards and geodetic eastwards (respectively) components of the ion drift (V_i , green) and neutral wind (V_n , purple) at 300 km. The ion drift is the $\vec{E} \times \vec{B}$ plasma drift velocity reconstructed from all AMISR LoS velocity measurements while the neutral winds are from HL-TWiM. Panel c shows the ion temperature calculated with Equation 1 at 300 km neglecting (green) and including (purple) the neutral winds, as well as the percent difference between the two (right hand axis). Panel d shows the full temperature profile calculated with Equation 1 using the RISR-N resolved ion velocities and HL-TWiM neutral winds. Panel e is the actual ion temperature directly measured by RISR-N.

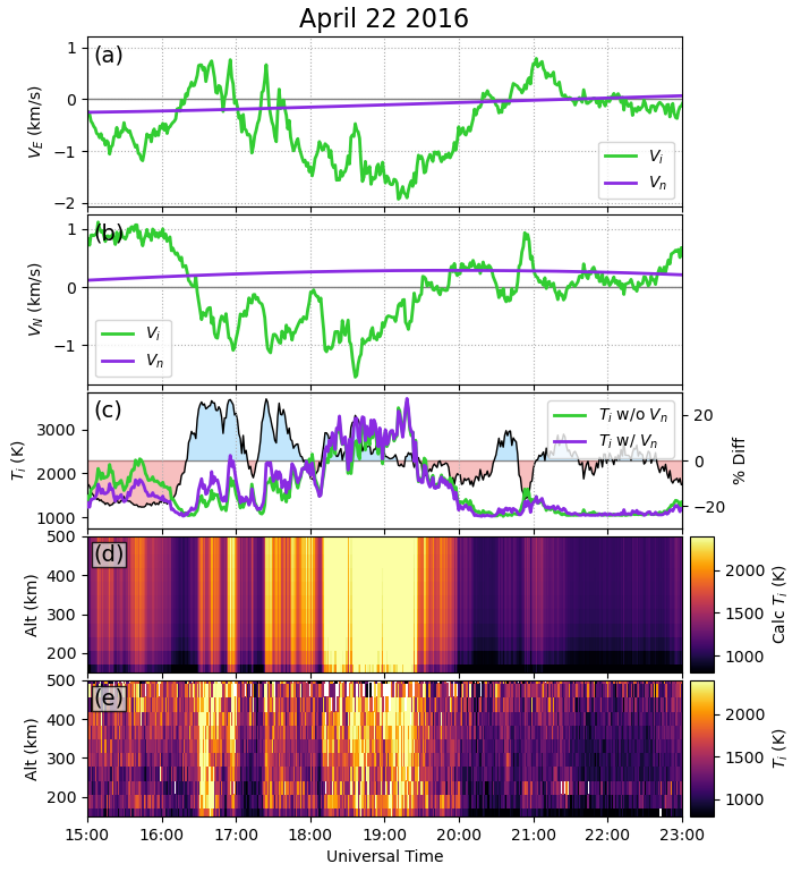


Figure 9. Comparison of calculated ion temperatures and observed ion temperatures for the April 2016 heating event. Figure format same as Figure 8

310 The neutral wind effects are generally of secondary importance compared to the
 311 magnitude of the ion drifts. For most of the May 30 heating event (except for a small
 312 period after 20:30 UT), neutral winds reduce the expected T_i by a small amount, gen-
 313 erally less than 10%. The April 22 2016 heating event on the other hand has two dis-
 314 tinct periods between 16:00–18:00 UT where neutral winds enhance T_i by over 20%. Neu-
 315 tral winds do not appear to significantly alter T_i during the main heating period on April
 316 22 2016 (18:00–19:30 UT).

317 The underestimation of the ion temperatures in the IPWM simulations can be largely
 318 explained by the underestimation of the input ion velocities. IPWM is solving a much
 319 more complex ion energy equation than Equation 1, which includes heat conduction along
 320 the field lines and ion-electron heating. Nonetheless, we can verify that Equation 1 is a
 321 reasonable approximation for the F-region solutions in IPWM. Figure 10 shows the com-
 322 parison of the IPWM results with the ion temperatures calculated from Equation 1 us-
 323 ing the SuperDARN and AMPERE velocities directly for the May 2014 event. Like IPWM,
 324 this calculation uses NRLMSISE-00 for the neutral temperature and ignores the neutral
 325 winds. Figures 10a shows the ion temperatures from IPWM, similar to Figures 2a, but
 326 focused on the same time periods shown in Figures 8. Figures 10b shows the ion tem-
 327 perature calculated from Equation 1 with the SuperDARN \vec{V}_i and neglecting \vec{V}_n . Pan-
 328 els c and d of Figure 10 are analogous to panels a and b, but use the AMPERE convec-
 329 tion patterns. Figure 11 shows the same calculations for the April 2016 events in the same
 330 format as Figure 10. The strong similarities between the T_i profiles from IPWM and cal-
 331 culated from Equation 1 in Figures 10 and 11 confirm that Equation 1 is a suitable ap-
 332 proximation of the full IPWM energy equation solution in the F-region. Neither the Su-
 333 perDARN nor the AMPERE T_i profiles match the T_i profiles RISR-N measured during
 334 these heating events though (Figures 8e and 9e). This is a strong indicator mesoscale
 335 flow channels RISR-N observed during these heating events are critical to these extreme
 336 heating event.

337 The IPWM simulations presented in this study are relatively low resolution. Nonethe-
 338 less, Equation 1 is an entirely local calculation that does not require gradients of any pa-
 339 rameters. The calculations shown in Figures 10 and 11 confirm that IPWM agrees with
 340 this local equation. We have also confirmed that the velocities in the IPWM after grid
 341 interpolations retain approximately the same magnitudes as the velocities directly from

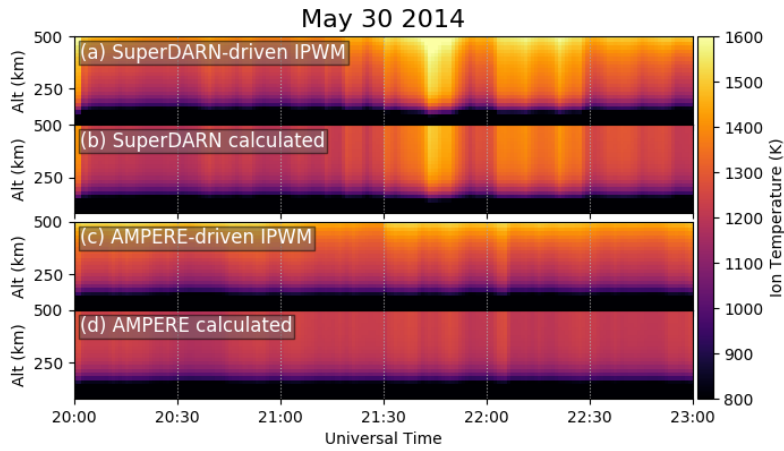


Figure 10. Comparison of ion temperatures produced by IPWM and those calculated with Equation 1 for the May 2014 heating event. Panels a and b are the ion temperature profiles from IPWM and Equation 1, respectively, using ion velocities from SuperDARN. Panels c and d are the ion temperature profiles from IPWM and Equation 1, respectively, using ion velocities from AMPERE.

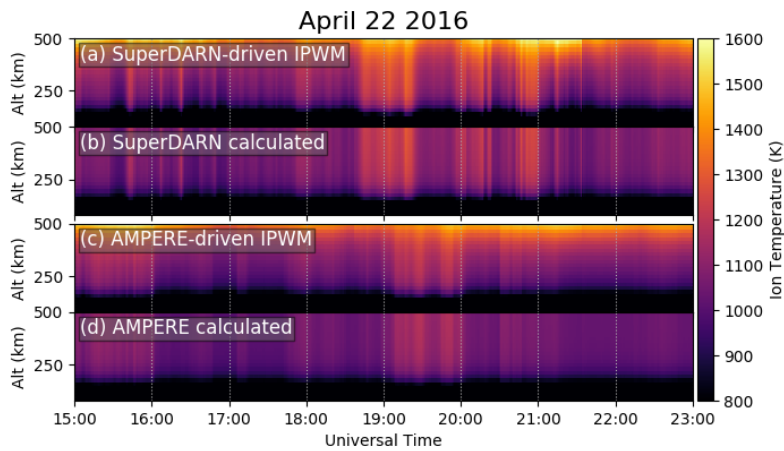


Figure 11. Comparison of ion temperatures produced by IPWM and those calculated with Equation 1 for the April 2016 heating event. Figure format is the same as Figure 10.

342 SuperDARN and AMPERE. Therefore, IPWM simulations at higher resolutions are not
343 expected to produce significantly different results for the ion temperatures.

344 Previous studies have shown good agreement between the SuperDARN and RISR-
345 N line-of-sight velocities (i.e. Koustov et al., 2016); however, there have rarely been com-
346 parisons specifically of strong flow events (≥ 1 km/s) like the ones that drove the heat-
347 ing events shown in Figures 8 and 9. Furthermore, both the SuperDARN and AMPERE
348 electric potential patterns that were fed into IPWM are designed to be global-scale maps
349 that show dynamics across the entire polar cap, and may struggle to reproduce extremely
350 localized structures like the ones observed by RISR-N during these heating events.

351 In addition to subgrid flows, small-scale precipitation structures may also be im-
352 port to localized heating events. Precipitation can modify the ionospheric conductivity
353 profile, altering how effective Joule heating is at different altitudes. Ovation Prime is a
354 purely empirical model, meaning that unlike the SuperDARN and AMPERE convection
355 data sets that were used, it does not assimilate real measurements from a particular time
356 so spectral characteristics are based exclusively off of historical statistics. In our simu-
357 lations, RISR-N is consistently poleward large precipitating fluxes in the cusp and in a
358 region where Ovation Prime predicts very little precipitation. The highly structured and
359 dynamic nature of the polar cap in general presents a significant challenge to statisti-
360 cal models, but it is difficult to quantify the uncertainty between the model output and
361 the true precipitation patterns. Northwards IMF conditions, such as those examined in
362 this study, have been associated with sun-aligned arcs, which are known to contain mesoscale
363 precipitation features (L. Zhu et al., 1997). Mesoscale precipitation features of scales not
364 captured by Ovation Prime do impact Joule heating in the auroral zone (Kosch et al.,
365 2011; Q. Zhu et al., 2018), but more research is required to determine if they have a sim-
366 ilar effect in the polar cap.

367 Finally, the thermodynamic ion temperature is the second moment of the full 3D
368 ion distribution function, whereas monostatic incoherent scatter radars can only mea-
369 sure the 1D marginal ion distribution function along the radar's line of sight (Akbari et
370 al., 2017). Standard AMISR fitting assumes an isotropic Maxwellian distributions of both
371 electrons and ions, in which case the 1D line of sight temperatures are the same as the
372 full 3D ion distribution function. This assumption starts to break down under strong rel-
373 ative ion-neutral drift, which can cause the distribution function to migrate from the as-

374 sumed isotropic distribution towards an anisotropic bi-Maxwellian or toroidal distribu-
 375 tion (St.-Maurice & Shunk, 1977; St.-Maurice & Schunk, 1979). For a bi-Maxwellian dis-
 376 tribution with different parallel and perpendicular ion temperatures, $T_{\parallel i}$ and $T_{\perp i}$, the
 377 ISR spectrum measured along a line of sight at an angle α away from the magnetic field
 378 will be identical to the ISR spectrum from an isotropic Maxwellian with effective tem-
 379 perature (Raman et al., 1981)

$$T_{1D} = T_{\parallel i} \cos^2 \alpha + T_{\perp i} \sin^2 \alpha, \quad (2)$$

380 which is generally different from the thermodynamic ion temperature for a bi-Maxwellian

$$T_i = \frac{1}{3} T_{\parallel i} + \frac{2}{3} T_{\perp i}. \quad (3)$$

381 For torodial ion distribution functions the ISR theory is far more complex, but the mod-
 382 ifications to the spectral shape are only detectable at angles significantly far away from
 383 parallel to the magnetic field (Winser et al., 1989; Akbari et al., 2017). For the heating
 384 events shown in this study which are characterized by strong V_i flows, anisotropic plasma
 385 distributions are a reasonable concern. All data-model comparisons in this study em-
 386 ployed high elevation beams with a small aspect angle with respect to the near-vertical
 387 magnetic field in the polar cap. Therefore, the measured ion temperatures presented in
 388 this work are essentially measurements of the parallel ion temperatures. For either bi-
 389 Maxwellian or torodial distributions that form due to frictional heating, the parallel tem-
 390 perature is expected to be less than the thermodynamic temperature, so the ion tem-
 391 peratures shown in Figures 2 and 5 can be thought of as a lower limit to the thermody-
 392 namic temperature (Akbari et al., 2017). This makes the fact that the modeled temper-
 393 atures were significantly lower than the observed (lower limit) temperatures all the more
 394 significant.

395 5 Conclusion

396 Joule heating is a significant factor in magnetosphere-ionosphere-thermosphere cou-
 397 pling and energy deposition in the polar cap ionosphere. Using a decade of RISR-N data,
 398 we performed a statistical analysis of the conditions under which temperature enhance-
 399 ments were most likely to occur, then attempted to model two notable events with IPWM.
 400 On average, the highest ion temperatures were observed under IMF Bz north conditions
 401 when the radar was in the noon sector. This is likely due to lobe reconnection driving
 402 fast sunwards flows polewards of the cusp. Data-driven IPWM simulations reproduced

403 some localized heating, but neither the timing nor the magnitude of the temperature en-
 404 hancements produced by the model matched the dramatic heating events observed in
 405 RISR-N data. Calculations using the locally measured ion velocities, however, were able
 406 to explain the observations. Furthermore, neutral wind effects are only of secondary im-
 407 portance given the typical magnitudes of the neutral wind velocities compared to the fast
 408 ion drifts observed in the polar cap (> 2 km/s). These results demonstrate that lobe
 409 reconnection can produce highly localized fast ion drifts that are very effective at pro-
 410 ducing frictional heating, and these localized drifts are not well resolved by current global
 411 electric field mapping techniques. More work is required to determine the origin of mesoscale
 412 structures in the polar cap and their impact on energy deposition.

413 **Acknowledgments**

414 This work is supported by NSF Grant AGS-1452191. Additionally, it is based upon work
 415 supported by the Resolute Bay Observatory which is a major facility funded by the Na-
 416 tional Science Foundation through cooperative agreement AGS-1840962 to SRI Inter-
 417 national. RISR-N data is available through the SRI International ISR Database at [https://](https://amisr.com/database/)
 418 amisr.com/database/. The resolvedvelocities code which is used to generate the $\vec{E} \times$
 419 \vec{B} plasma drift velocities from AMISR data is publicly available at [http://doi.org/](http://doi.org/10.5281/zenodo.4451504)
 420 [10.5281/zenodo.4451504](http://doi.org/10.5281/zenodo.4451504). The 5-minute-integrated RISR-N database used for the sta-
 421 tistical study, specific RISR-N data files used in the event studies, IPWM input and con-
 422 figuration files, and scripts for generating the results and plots shown in this paper have
 423 also been made publicly available (<https://doi.org/10.5281/zenodo.4453389>). IPWM
 424 output are available at <https://doi.org/10.5281/zenodo.4451249>, [http://doi.org/](http://doi.org/10.5281/zenodo.4452793)
 425 [10.5281/zenodo.4452793](http://doi.org/10.5281/zenodo.4452793), <http://doi.org/10.5281/zenodo.4453485>, and [http://](http://doi.org/10.5281/zenodo.4453495)
 426 doi.org/10.5281/zenodo.4453495. The analysis code is also available in a configured
 427 Resen bucket (Bhatt et al., 2020), also at <https://doi.org/10.5281/zenodo.4453389>.
 428 OMNI data was retrieved through spacepy (Morley et al., 2011).

429 **References**

- 430 Aikio, A. T., Cai, L., & Nygrén, T. (2012). Statistical distribution of height-
 431 integrated energy exchange rates in the ionosphere. *J. Geophys. Res.*, *117*. doi:
 432 [10.1029/2012JA018078](https://doi.org/10.1029/2012JA018078)
- 433 Aikio, A. T., & Selkälä, A. (2009). Statistical properties of joule heating rate,

- 434 electric field and conductances at high latitudes. *Ann. Geophysicae*, *27*, 2661–
435 2673. doi: 10.5194/angeo-27-2661-2009
- 436 Akbari, H., Goodwin, L. V., Swoboda, J., St.-Maurice, J.-P., & Semeter, J. L.
437 (2017). Extreme plasma convection and frictional heating of the ionosphere:
438 ISR observations. *J. Geophys. Res. Space Physics*, *122*, 7581–7598. doi:
439 10.1002/2017JA023916
- 440 Anderson, B. J., Korth, H., Waters, C. L., Green, D. L., Merkin, V. G., Barnes,
441 R. L., & Dyrund, L. P. (2014). Development of large-scale birkeland cur-
442 rents determined from the active magnetosphere and planetary electrody-
443 namics response experiment. *Geophys. Res. Lett.*, *41*, 3017–3025. doi:
444 10.1002/2014GL059941
- 445 Anderson, B. J., Takahashi, K., & Toth, B. A. (2000). Sensing global Birkeland
446 currents with Iridium engineering magnetometer data. *Geophys. Res. Lett.*,
447 *27*(24), 4045–4048.
- 448 Bahcivan, H., Tsunoda, R., Nicolls, M., & Heinselman, C. (2010). Initial ionospheric
449 observations made by the new Resolute incoherent scatter radar and compari-
450 son to solar wind IMF. *Geophys. Res. Lett.*, *37*. doi: 10.1029/2010GL043632
- 451 Bhatt, A., Valentic, T., Reimer, A., Lamarche, L., Reyes, P., & Cosgrove, R. (2020).
452 Reproducible software environment: a tool enabling computational repro-
453 ducibility in geospace sciences and facilitating collaboration. , *10*, 12. doi:
454 10.1051/swsc/2020011
- 455 Billett, D. D., Wild, J. A., Grocott, A., Aruliah, A. L., Ronksley, A. M., Walach,
456 M.-T., & Lester, M. (2019). Spatially resolved neutral wind response times
457 during high geomagnetic activity above Svalbard. *J. Geophys. Res. Space
458 Physics*, *124*, 6950–6960. doi: 10.1029/2019JA026627
- 459 Burke, W. J., Kelley, M. C., Sagalyn, R. C., Smiddy, M., & Lai, S. T. (1979). Polar
460 cap electric field structures with a northwards interplanetary magnetic field.
461 *Geophys. Res. Lett.*, *6*(1), 21–24.
- 462 Cai, L., Aikio, A. T., & Nygrén, T. (2014). Solar wind effect on Joule heating in the
463 high-latitude ionosphere. *J. Geophys. Res. Space Physics*, *119*, 10440–10455.
464 doi: 10.1002/2014JA020269
- 465 Chen, Y.-J., & Heelis, R. A. (2018). Mesoscale plasma convection perturbations in
466 the high-latitude ionosphere. *J. Geophys. Res. Space Physics*, *123*, 7609–7620.

- 467 doi: 10.1029/2018JA025716
- 468 Chisham, G., Lester, M., Milan, S. E., Freeman, M. P., Bristow, W. A., Grocott,
469 A., ... Walker, A. D. M. (2007). A decade of the Super Dual Auroral Radar
470 Network (SuperDARN): scientific achievements, new techniques and future
471 directions. *Surv. Geophys.*, *28*, 33–109. doi: 10.1007/s10712-007-9017-8
- 472 Chun, F. K., Knipp, D. J., McHarg, M. G., Lacey, J. R., Lu, G., & Emery, B. A.
473 (2002). Joule heating patterns as a function of polar cap index. *J. Geophys.*
474 *Res.*, *107*(A7), 1119. doi: 10.1029/2001JA000246
- 475 Clauer, C. R., Xu, Z., Maimaiti, M., Ruohoneimi, J. M., Scales, W., Hartinger,
476 M. D., ... Lopez, R. E. (2016). Investigation of a rare event where the polar
477 ionospheric reverse convection potential does not saturate during a period of
478 extreme northward IMF solar wind driving. *J. Geophys. Res. Space Physics*,
479 *121*(6), 5422–5435. doi: 10.1002/2016JA022557
- 480 Cousins, E. D. P., Matsuo, T., & Richmond, A. D. (2015). Mapping high-latitude
481 ionospheric electrodynamics with SuperDARN and AMPERE. *J. Geophys.*
482 *Res. Space Physics*, *120*, 5854–5870. doi: 10.1002/2014JA020463
- 483 Cousins, E. D. P., & Shepherd, S. G. (2010). A dynamical model of high-latitude
484 convection derived from SuperDARN plasma drift measurements. *J. Geophys.*
485 *Res.*, *115*. doi: 10.1029/2010JA016017
- 486 Cowley, S. W. H. (1983). Interpretation of observed relations between solar wind
487 characteristics and effects at ionospheric altitudes. In B. Hultqvist & T. Hag-
488 fors (Eds.), *High-latitude space plasma physics* (Vol. 54, pp. 225–249). Boston,
489 MA: Springer. doi: 10.1007/978-1-4613-3652-5_13
- 490 Dhadly, M. S., Emmert, J. T., Drob, D. P., Conde, M. G., Aruliah, A., Doornbos,
491 E., ... Ridley, A. J. (2019). HL-TWiM empirical model of high-latitude upper
492 thermospheric winds. *J. Geophys. Res. Space Physics*, *124*, 10592–10618. doi:
493 10.1029/2019JA027188
- 494 Dungey, J. W. (1961). Interplanetary magnetic field and the auroral zones. *Phys.*
495 *Rev. Lett.*, *6*, 47–48.
- 496 Emmert, J. T., Hernandez, G., Jarvis, M. J., Niciejewski, R. J., Sipler, D. P., & Ven-
497 nerstrom, S. (2006). Climatologies of nighttime upper thermospheric winds
498 measured by ground-based fabry-perot interferometers during geomagnetically
499 quiet conditions: 2. high-latitude circulation and interplanetary magnetic field

- 500 dependence. *J. Geophys. Res.*, *111*. doi: 10.1029/2006JA011949
- 501 Fang, X., Randall, C. E., Lummerzheim, D., Solomon, S. C., Mills, M. J., Marsh,
502 D. R., ... Lu, G. (2008). Electron impact ionization: A new parameter-
503 ization for 100 eV to 1 MeV electrons. *J. Geophys. Res.*, *113*. doi:
504 10.1029/2008JA013384
- 505 Farugia, C. J., Lund, E. J., Sandholt, P. E., Wild, J. A., Coley, S. W. H., Balogh,
506 A., ... Rème, H. (2004). Pulsed flows at the high-altitude cusp polewards
507 boundary, and associated ionospheric convection and particle signatures, dur-
508 uring a Cluster-FAST-SuperDARN-Søndrestøm conjunction under a southwest
509 IMF. *Ann. Geophysicae*, *22*, 2891-2905.
- 510 Förster, M., Haaland, S. E., Paschmann, G., Quinn, J. M., Torbert, R. B., Vaith, H.,
511 & Kletzing, C. A. (2008). High-latitude plasma convection during northward
512 IMF as derived from in-situ magnetospheric Cluster EDI measurements. *Ann.*
513 *Geophysicae*, *26*, 2685–2700. doi: 10.5194/angeo-26-2685-2008
- 514 Förster, M., Rentz, S., Köhler, W., Liu, H., & Haaland, S. (2008). IMF depen-
515 dence of high-latitude thermospheric wind pattern derived from CHAMP
516 cross-track measurements. *Ann. Geophysicae*, *26*, 1581–1595. doi:
517 10.5194/angeo-26-1581-2008
- 518 Foster, J. C., & St.-Maurice, J.-P. (1983). Joule heating at high latitudes. *J. Geo-*
519 *phys. Res.*, *88*(A6), 4885–4896.
- 520 Fujii, R., Nozawa, S., & Buchert, S. C. (1999). Statistical characteristics of electro-
521 magnetic energy transfer between the magnetosphere, the ionosphere, and the
522 thermosphere. *J. Geophys. Res.*, *104*(A2), 2357–2365.
- 523 Greenwald, R. A., Baker, K. B., Dudeney, J. R., Pinnock, M., Jones, T. B., Thomas,
524 E. C., ... Yamagishi, H. (1995). DARN/SUPERDARN: A global view of
525 the dynamics of high-latitude convection. *Space Sci. Rev.*, *71*, 761–796. doi:
526 10.1007/BF00751350
- 527 Hardy, D. A., Holeman, E. G., Burke, W. J., Gentile, L. C., & Bounar, K. H.
528 (2008). Probability distributions of electron precipitation at high magnetic
529 latitudes. *J. Geophys. Res.*, *113*. doi: 10.1029/2007JA012746
- 530 Hardy, D. A., Schmitt, L. K., Gussenhoven, M. S., Yeh, H. C., Schumaker, T. L.,
531 Huber, A., & Pantazi, J. (1984, November). *Precipitating electron and ion*
532 *detectors (SSJ/4) for the block 5D/flights 6–10 DMSP satellites: Calibration*

- 533 *and data presentation* (Tech. Rep. No. AFGL-TR-84-0317 ERP 902). Hanscom
534 AFB, MA: Air Force Geophysics Laboratory.
- 535 Heinselman, C. J., & Nicolls, M. J. (2008). A Bayesian approach to electric field
536 and E-region neutral wind estimation with the Poker Flat Advanced Modular
537 Incoherent Scatter Radar. *Radio Sci.*, *43*. doi: 10.1029/2007RS003805
- 538 Howarth, A., & Yau, A. W. (2008). The effects of IMF and convection on thermal
539 ion outflow in magnetosphere-ionosphere coupling. *J. Atmos. Sol. Terr. Phys.*,
540 *70*, 2132–2143. doi: 10.1016/j.jastp.2008.08.008
- 541 Kelly, J., & Heinselman, C. J. (2009). Initial results for Poker Flat Incoherent Scatter
542 Radar (PFISR). *J. Atmos. Sol. Terr. Phys.*, *71*, 635. doi: 10.1016/j.jastp
543 .2009.01.009
- 544 Knipp, D. J., Emery, B. A., Engebretson, M., Li, X., McAllister, A. H., Mukai, T.,
545 ... Wilkinson, P. (1998). An overview of the early November 1993 geomag-
546 netic storm. *J. Geophys. Res.*, *103*(A11), 26197–26220.
- 547 Kosch, M. J., Yiu, I., Anderson, C., Tsuda, T., Ogawa, Y., Nozawa, S., ... Wild,
548 J. A. (2011). Mesoscale observations of joule heating near an auroral arc and
549 ion-neutral collision frequency in the polar cap E region. *J. Geophys. Res.*,
550 *116*. doi: 10.1029/2010JA016015
- 551 Koustov, A. V., Lavoie, D. B., & Varney, R. H. (2016). On the consistency of the
552 SuperDARN radar velocity and $E \times B$ plasma drift. *Radio Sci.*, *51*, 1792–1805.
553 doi: 10.1002/2016RS006134
- 554 Li, K., Haaland, S., Eriksson, A., André, M., Engwall, E., Wei, Y., ... Ren, Q. Y.
555 (2012). On the ionospheric source region of cold ion outflow. *Geophys. Res.*
556 *Lett.*, *39*. doi: 10.1029/2012GL053297
- 557 Li, K., Haaland, S., Eriksson, A., André, M., Engwall, E., Wei, Y., ... Ren, Q. Y.
558 (2013). Transport of cold ions from the polar ionosphere to the plasma sheet.
559 *J. Geophys. Res. Space Physics*, *118*, 5467–5477. doi: 10.1002/jgra.50518
- 560 Lockwood, M., Moen, J., van Eyken, A. P., Davies, J. A., Oksavik, K., & McCrea,
561 I. W. (2005). Motion of the dayside polar cap boundary during substorm
562 cycles: I. observations of pulses in the magnetopause reconnection rate. *Ann.*
563 *Geophysicae*, *23*, 3495–3511. doi: 10.5194/angeo-23-3495-2005
- 564 Lu, G., Richmond, A. D., Lühr, H., & Paxton, L. (2016). High-latitude energy in-
565 put and its impact on the thermosphere. *J. Geophys. Res. Space Physics*, *121*,

- 566 7108–7124. doi: 10.1002/2015JA022294
- 567 McHarg, M., Chun, F., Knipp, D., Lu, G., Emery, B., & Ridley, A. (2005). High-
568 latitude Joule heating response to IMF inputs. *J. Geophys. Res.*, *110*. doi: 10
569 .1029/2004JA010949
- 570 Moen, J., Lockwood, M., Oksavik, K., Carlson, H. C., Denig, W. F., van Eyken,
571 A. P., & McCrea, I. W. (2004). The dynamics and relationship of precipita-
572 tion, temperature and convection boundaries in the dayside auroral ionosphere.
573 *Ann. Geophysicae*, *22*, 1973–1987. doi: 10.5194/angeo-22-1973-2004
- 574 Moore, T. E., & Horwitz, J. L. (2007). Stellar ablation of planetary atmospheres.
575 *Reviews of Geophysics*, *45*. doi: 10.1029/2005RG000194
- 576 Morley, S. K., Koller, J., Welling, D. T., Larsen, B. A., Henderson, M. G., & Niehof,
577 J. T. (2011). Spacepy - a python-based library of tools for the space sciences.
578 In *Proceedings of the 9th python in science conference (scipy 2010)*. Austin,
579 TX.
- 580 Newell, P. T., Sotirelis, T., & Wing, S. (2009). Diffuse, monoenergetic, and broad-
581 band aurora: The global precipitation budget. *J. Geophys. Res. Space Physics*,
582 *114*(A9). doi: 10.1029/2009JA014326
- 583 Olsson, A., Janhunen, P., Ivchenko, N., & Blomberg, L. G. (2004). Statistics of joule
584 heating in the auroral zone and polar cap using Astrid-2 satellite Poynting
585 flux. *Ann. Geophysicae*, *22*, 4133–4142.
- 586 Østgaard, N., Germany, G., Stadsnes, J., & Vondrak, R. R. (2002). Energy anal-
587 ysis of substorms based on remote sensing techniques, solar wind measure-
588 ments, and geomagnetic indices. *J. Geophys. Res.*, *107*(A9), 1233. doi:
589 10.1029/2001JA002002
- 590 Palmroth, M., Janhunen, P., Pulkkinen, T. I., Aksnes, A., Lu, G., Østgaard, N., . . .
591 Germany, G. A. (2005). Assessment of ionosphere Joule heating by GUMICS-4
592 MHD simulation, AMIE, and satellite-based statistics: towards a synthesis.
593 *Ann. Geophysicae*, *23*, 2051–2068. doi: 10.5194/angeo-23-2051-2005
- 594 Peterson, W. K., Andersson, L., Callahan, B., Elkington, S. R., Winglee, R. W.,
595 Scudder, J. D., & Collin, H. L. (2009). Geomagnetic activity dependence of
596 O^+ in transit from the ionosphere. *J. Atmos. Sol. Terr. Phys.*, *71*, 1623–1629.
- 597 Picone, J. M., Hedin, A. E., Drob, D. P., & Aikin, A. C. (2002). NRLMSISE-00 em-
598 pirical model of the atmosphere: Statistical comparisons and scientific issues.

- 599 *J. Geophys. Res.*, *107*(A12), 1468. doi: 10.1029/2002JA009430
- 600 Prikryl, P., Provan, G., McWilliams, K. A., & Yeoman, T. K. (2002). Ionospheric
601 cusp flows pulsed by solar wind Alfvén waves. *Ann. Geophysicae*, *20*, 161–174.
- 602 Provan, G., Milan, S. E., Lester, M., Yeoman, T. K., & Khan, H. (2002). Simul-
603 taneous observations of the ionospheric footprint of flux transfer events and
604 dispersed ion signatures. *Ann. Geophysicae*, *20*, 281–287.
- 605 Raman, R. S. V., St-Maurice, J.-P., & Ong, R. S. B. (1981). Incoherent scatter-
606 ing of radar waves in the auroral ionosphere. *J. Geophys. Res. Space Physics*,
607 *86*(A6), 4751–4762. doi: 10.1029/JA086iA06p04751
- 608 Reiff, P. H., & Heelis, R. A. (1994). Four cells or two? Are four convection cells
609 really necessary? *J. Geophys. Res. Space Physics*, *99*(A3), 3955–3959. doi: 10
610 .1029/93JA01992
- 611 Richards, P. G., Woods, T. N., & Peterson, W. K. (2006). HEUVAC: A new high
612 resolution solar EUV proxy model. *Advances in Space Research*, *37*, 315–322.
613 doi: 10.1016/j.asr.2005.06.031
- 614 Richmond, A. D., & Kamide, Y. (1988). Mapping electrodynamic features of the
615 high-latitude ionosphere from localized observations: Technique. *J. Geophys.*
616 *Res. Space Physics*, *93*(A6), 5741–5759. doi: 10.1029/JA093iA06p05741
- 617 Richmond, A. D., Lathuillière, C., & Vennerstroem, S. (2003). Winds in the high-
618 latitude lower thermosphere: Dependence on the interplanetary magnetic field.
619 *J. Geophys. Res.*, *108*(A2), 1066. doi: 10.1029/2002JA009493
- 620 Shen, Y., Knudsen, D. J., Burchill, J. K., Howarth, A., Yau, A., Redmon, R. J., ...
621 Nicolls, M. J. (2016). Strong ambipolar-driven ion upflow within the cleft ion
622 fountain during low geomagnetic activity. *J. Geophys. Res. Space Physics*,
623 *121*(7), 6950–6969. doi: 10.1002/2016JA022532
- 624 Skjæveland, Å., Moen, J., & Carlson, H. C. (2011). On the relationship between flux
625 transfer events, temperature enhancements, and ion upflow events in the cusp
626 ionosphere. *J. Geophys. Res.*, *116*. doi: 10.1029/2011JA016480
- 627 St.-Maurice, J.-P., & Hanson, W. B. (1982). Ion frictional heating at high lati-
628 tudes and its possible use for an in situ determination of neutral thermospheric
629 winds and temperatures. *J. Geophys. Res.*, *87*(A9), 7580–7602.
- 630 St.-Maurice, J.-P., & Schunk, R. W. (1979). Ion velocity distributions in the high-
631 latitude ionosphere. *Rev. Geophys. Space Physics*, *17*(1), 99–134. doi: 10.1029/

- 632 RG017i001p00099
- 633 St.-Maurice, J.-P., & Shunk, R. W. (1977). Auroral ion velocity distributions for a
634 polarization collision model. *Planet. Space Sci.*, *25*(3), 243–260. doi: 10.1016/
635 0032-0633(77)90135-0
- 636 Tanskanen, E., Pulkkinen, T. I., & Koskinen, H. E. J. (2002). Substorm energy bud-
637 get durring low and high solar activity: 1997 and 1999 compared. *J. Geophys.*
638 *Res.*, *107*(A6), 1086. doi: 10.1029/2001JA900153
- 639 Thayer, J. P., & Semeter, J. (2004). The convergence of magnetospheric energy flux
640 in the polar atmosphere. *J. Atmos. Sol. Terr. Phys.*, *66*, 807–824.
- 641 Thayer, J. P., Vickrey, J. F., Heelis, R. A., & Gary, J. B. (1995). Interpretation and
642 modeling of the high-latitude electromagnetic energy flux. *J. Geophys. Res.*,
643 *100*, 19715–19728.
- 644 Thomas, E. G., & Sheperd, S. G. (2018). Statistical patterns of ionospheric con-
645 vection derived from mid-latitude, high-latitude, and polar SuperDARN HF
646 radar observations. *J. Geophys. Res. Space Physics*, *123*, 3196–3216. doi:
647 10.1002/2018JA025280
- 648 Varney, R. H., Solomon, S. C., & Nicolls, M. J. (2014). Heating of the sunlit po-
649 lar cap ionosphere by reflected photoelectrons. *J. Geophys. Res. Space Physics*,
650 *119*, 8660–8684. doi: 10.1002/2013JA019378
- 651 Varney, R. H., Wiltberger, M., & Lotko, W. (2015). Modeling the interaction
652 between convection and nonthermal ion outflows. *J. Geophys. Res. Space*
653 *Physics*, *120*, 2353–2362. doi: 10.1002/2014JA020769
- 654 Varney, R. H., Wiltberger, M., Zhang, B., Lotko, W., & Lyon, J. (2016). Influence
655 of ion outflow in coupled geospace simulations: 1. Physics-based ion outflow
656 model development and sensitivity study. *J. Geophys. Res. Space Physics*, *121*,
657 9671–9687. doi: 10.1002/2016JA022777
- 658 Wahlund, J.-E., Opgenoorth, H. J., Häggström, I., Winsor, K. J., & Jones, G. O. L.
659 (1992). EISCAT observations of topside ionospheric ion outflows during auro-
660 ral activity: Revisited. *J. Geophys. Res.*, *97*(A3), 3019–3037.
- 661 Waters, C. L., Anderson, B. J., & Liou, K. (2001). Estimation of global field aligned
662 currents using the Iridium system magnetometer data. *Geophys. Res. Lett.*,
663 *28*(11), 2165–2168.
- 664 Winsor, K. J., Lockwood, M., Jones, G. O. L., & Suvanto, K. (1989). Observa-

- 665 tions of nonthermal plasmas at different aspect angles. *J. Geophys. Res. Space*
666 *Physics*, *94*(A2), 1439-1449. doi: 10.1029/JA094iA02p01439
- 667 Yau, A. W., Howarth, A., Pererson, W. K., & Abe, T. (2012). Transport of thermal-
668 energy ionospheric oxygen (O^+) ions between the ionosphere and the plasma
669 sheet and ring current at quiet times preceding magnetic storms. *J. Geophys.*
670 *Res.*, *117*. doi: 10.1029/2012JA017803
- 671 Zhang, B., Brambles, O., Lotko, W., Dunlap-Shohl, W., Smith, R., Wiltberger, M.,
672 & Lyon, J. (2013). Predicting the location of polar cusp in the Lyon-Fedder-
673 Mobarry global magnetosphere simulation. *J. Geophys. Res. Space Physics*,
674 *118*, 6327–6337. doi: 10.1002/jgra.50565
- 675 Zhang, X. X., Wang, C., Chen, T., Wang, Y. L., Tan, A., Wu, T. S., ... Wang, W.
676 (2005). Global patterns of Joule heating in the high-latitude ionosphere. *J.*
677 *Geophys. Res.*, *110*. doi: doi:10.1029/2005JA011222
- 678 Zhu, L., Shunk, R. W., & Sojka, J. J. (1997). Polar cap arcs: A review. *J. Atmos.*
679 *Sol. Terr. Phys.*, *59*(10), 1087–1126. doi: 10.1029/2018JA025771
- 680 Zhu, Q., Deng, Y., Richmond, A., & Maute, A. (2018). Small-scale and mesoscale
681 variabilities in the electric field and particle precipitation and their impacts on
682 Joule heating. *J. Geophys. Res. Space Physics*, *123*, 9862–9872.